

# GeoGround : A Unified Large Vision-Language Model for Remote Sensing Visual Grounding

Yue Zhou<sup>1</sup>      Mengcheng Lan<sup>1</sup>      Xiang Li<sup>2</sup>      Yiping Ke<sup>3</sup>      Jiang Xue<sup>4</sup>

Litong Feng<sup>5\*</sup>      Wayne Zhang<sup>5</sup>

<sup>1</sup>S-Lab, Nanyang Technological University, <sup>2</sup>CS, University of Reading

<sup>3</sup>CCDS, Nanyang Technological University, <sup>4</sup>SEIEE, Shanghai Jiaotong University

<sup>5</sup>SenseTime Research

## Abstract

Remote sensing (RS) visual grounding aims to use natural language expression to locate specific objects (in the form of the bounding box or segmentation mask) in RS images, enhancing human interaction with intelligent RS interpretation systems. Early research in this area was primarily based on horizontal bounding boxes (HBBs), but as more diverse RS datasets have become available, tasks involving oriented bounding boxes (OBBs) and segmentation masks have emerged. In practical applications, different targets require different grounding types: HBB can localize an object’s position, OBB provides its orientation, and mask depicts its shape. However, existing specialized methods are typically tailored to a single type of RS visual grounding task and are hard to generalize across tasks. In contrast, large vision-language models (VLMs) exhibit powerful multi-task learning capabilities but struggle to handle dense prediction tasks like segmentation. This paper proposes *GeoGround*, a novel framework that unifies support for HBB, OBB, and mask RS visual grounding tasks, allowing flexible output selection. Rather than customizing the architecture of VLM, our work aims to elegantly support pixel-level visual grounding output through the *Text-Mask* technique. We define prompt-assisted and geometry-guided learning to enhance consistency across different signals. To support model training, we present *refGeo*, a large-scale RS visual instruction-following dataset containing 161k image-text pairs. Experimental results show that *GeoGround* demonstrates strong performance across four RS visual grounding tasks, matching or surpassing the performance of specialized methods on multiple benchmarks. Code available at <https://github.com/zytx121/GeoGround>.

\*Corresponding author.

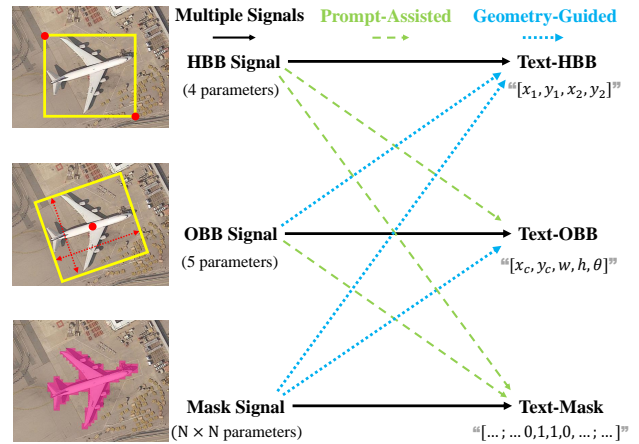


Figure 1. An overview of the hybrid supervision of GeoGround.

## 1. Introduction

In the remote sensing (RS) community, the early visual grounding task [26, 37] specifically refers to the location of specific objects in terms of horizontal bounding boxes (HBBs), given a satellite image and related text query. With increasing availability of the RS dataset [12, 25, 34], researchers have started to use oriented bounding boxes (OBBs) [9] or segmentation masks [36] to more accurately depict the referred objects. RS visual grounding enables humans to interact with computers in a more intuitive manner, which has enormous promise for improving the efficiency of intelligent RS interpretation systems [29].

Most existing RS visual grounding [26, 37] and referring segmentation [16, 36] methods are designed with task-specific modules and loss functions. Models based on HBB typically adopt loss functions in object detection tasks, such as Smooth L1, while models based on mask often use loss functions from semantic segmentation tasks, such as pixel-level cross-entropy. Enabling multi-task learning [27] in

such models not only requires modifications to the network but also necessitates careful tuning of the weights between various loss functions, making the process quite challenging. Although large vision-language models (VLMs) [1, 2, 5, 15] can support multiple multimodal RS tasks simultaneously by using a unified text regression loss function, they struggle with pixel-level tasks such as segmentation. This is because, as the output module of a VLM, the large language model (LLM) can only generate textual data and cannot produce output in the image modality [4].

To address these challenges, we propose GeoGround, an elegant VLM that seamlessly unifies visual grounding tasks at the HBB, OBB, and pixel-level RS. Our key innovation lies in converting box-level and pixel-level signals into textual sequences, enabling the model to train diverse visual grounding tasks within a unified training pipeline. Specifically, we propose the Text-Mask paradigm, which distills and compresses the information embedded in the mask into a compact text sequence that can be efficiently learned by VLMs. Additionally, we introduce hybrid supervision, as shown in Fig. 1, which incorporates prompt-assisted learning (PAL) and geometry-guided learning (GGL) to fine-tune the model using three types of signals, ensuring output consistency and enhancing the model’s understanding of the relationships between different grounding types.

To support GeoGround training and promote the development of visual RS grounding, we introduce refGeo, a large-scale RS visual grounding instruction-following dataset. refGeo consolidates four existing visual grounding datasets from RS [9, 13, 26, 37] and introduces a new aerial vehicle visual grounding dataset (AVVG). AVVG extends traditional 2D visual grounding to a 3D context, enabling VLMs to perceive 3D space from 2D aerial imagery. For each referred object, we provide HBB, OBB, and mask, with the latter automatically generated by the SAM [8].

In summary, our key contributions are as follows:

- We propose GeoGround, a novel VLM framework that unifies box-level and pixel-level RS visual grounding tasks while maintaining its inherent dialogue and image understanding capabilities.
- We introduce refGeo, the largest RS visual grounding instruction-following dataset, consisting of 161k image-text pairs and 80k RS images, including a new 3D-aware aerial vehicle visual grounding dataset.
- We conduct extensive experiments on various RS visual grounding tasks, providing valuable insights for future RS VLM research and opening new avenues for research in RS visual grounding.

## 2. Related Work

**Remote Sensing Referring Detection and Segmentation.** Compared to multimodal tasks like image captioning [14, 40], text-image retrieval [19], and visual question answer-

ing (VQA) [17] in RS, research on referring detection is a novel task with limited research. It was first introduced by GeoVG [36], which proposed the first RS visual grounding dataset. MGVLV [37] leverages multiscale visual features and multi-granularity textual embeddings to address the scale variation in RS images. RS referring segmentation is also in its early stages due to the challenges mentioned earlier. It was first introduced by RefSegRS [36], which proposed a new dataset and baseline model. Recently, the transformer-based method RMSIN [16] proposed an adaptive rotated convolution to tackle the issues arising from the scale variation and orientations prevalent in aerial imagery. However, these two types of models have always been studied separately, hindering progress in the field. In this paper, we unify these two tasks within a single framework, allowing them to share data and architecture.

**Generalist VLMs.** Several efforts have been made to equip VLMs with visual grounding capabilities in the domain of natural images [3, 4, 10, 22, 30, 33, 38]. For instance, Shikra [3] directly textualizes HBB to support visual grounding tasks, but its discrete coordinate output is inadequate for pixel-level tasks. LISA [10] addresses this by incorporating a mask decoder to handle the RES task, while NExt-Chat [38] expands this paradigm by adding two decoders to support both box and mask outputs. In contrast, our approach elegantly unifies box-level and pixel-level visual grounding tasks based on general-purpose VLM, eliminating the need for additional encoders or decoders.

**Remote Sensing VLMs** have shown promising results in image-level tasks such as scene classification, image captioning, and VQA [13, 31, 41]. However, works [9, 20, 21, 39] on object-level tasks such as RS visual grounding remains comparatively unexplored. GeoChat [9] constructs a new dataset using OBB annotation and proposes the first RS visual grounding model based on OBB. However, the unsuitable choice of OBB angle representation limits its performance. Moreover, the small scale of the RS visual grounding dataset selected by LHRS-Bot [20] and H<sup>2</sup>RSVLM [21] hampers their generalization ability on this task. To address these issues, we introduce refGeo, a large-scale RS visual grounding dataset with multi-type annotations. For each type of annotation, we perform a systematic exploration to identify the most suitable format.

## 3. GeoGround

The architecture of GeoGround is highly streamlined, consisting of only a visual encoder (CLIP-ViT [23]), a connector (two-layer MLPs), and an LLM (Vicuna 1.5 [43]), without introducing additional encoders or decoders. Fig. 2 illustrates the framework of our proposed model, which can

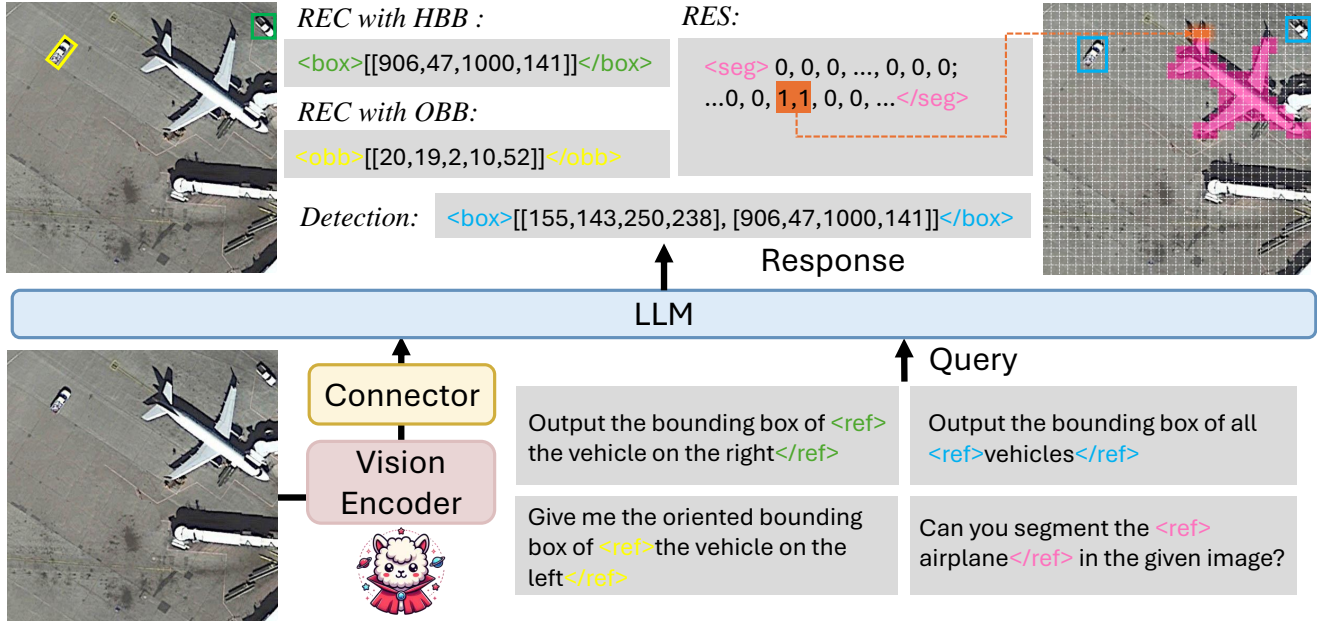


Figure 2. An overview of GeoGround – the first model to unify box-level and pixel-level visual grounding tasks in remote sensing.

flexibly output HBBs, OBBs, or segmentation masks based on user instructions. In addition to single-object outputs, the model is also capable of handling multi-object outputs.

### 3.1. Signal Textualization

To train three types of visual grounding tasks with a unified data pipeline, we textualize the three grounding supervision signals into three corresponding text strings. We refer to this process as signal textualization, which serves as the cornerstone of our method.

**Text-HBB and Text-OBB** are generated by directly converting numerical coordinates into text sequences [3]. Specifically, the coordinates are normalized, multiplied by the resolution, and then rounded. The resulting numbers are separated by commas and enclosed in parentheses, as illustrated in Fig. 2. In GeoGround, we set the resolution of the Text-HBB to 1000, allowing for more precise localization of small objects in RS images. Compared to Text-HBB, Text-OBB includes an additional angle parameter. Since there are various angle representations of OBB, the meaning of the first four numbers differs. Based on experiments, we adopt the long side 90-degree representation [44] in GeoGround, where the angle ranges from 0 to 90 degrees. To ensure that these values align with the angle in terms of range, we set the resolution of Text-OBB to 100 by default.

**Text-Mask** should be generated by converting the mask into text sequences. However, this conversion is challenging due to the inherent differences between the image and

text modalities. Inspired by Text4Seg [11], we propose a novel Text-Mask paradigm that treats the segmentation mask as text. Specifically, we downsample the mask into an  $N \times N$  grid, where the object region is labeled 1 and the background region 0, as shown in Fig. 2. This results in a binary matrix that approximately represents the object’s location and shape. Higher resolution improves shape precision but results in longer text sequences, increasing training difficulty and slowing inference. To further reduce the token length required to represent a mask, we employ R-RLE [11] to compress redundant text sequences. It significantly reduces the length of Text-Mask and accelerates inference speed, without compromising performance. For RS visual grounding datasets, a resolution of 32 enables Text-Mask to effectively represent most objects.

### 3.2. Hybrid Supervision

We propose a hybrid supervision that simultaneously utilizes Text-HBB, Text-OBB, and Text-Mask to comprehensively enhance the visual grounding capabilities of VLMs. First, we adopt a basic supervised learning paradigm to train three types of visual grounding tasks, as follows:

$$t = \mathcal{F}(\mathbf{I}, \mathbf{q}) \quad (1)$$

where  $\mathcal{F}$  denotes the LLM of our model,  $\mathbf{I}$  represents the image embedding,  $\mathbf{q}$  represents the query text embedding.  $t$  can represent the Text-HBB, Text-OBB, and Text-Mask, respectively. Next, we define the following two auxiliary tasks to establish connections between the different signals.

**Prompt-Assisted Learning:** Output the oriented bounding box of `<ref>obj</ref><box>[[400,400,600,600]]</box>`  
**Response:** `<obb>[[500,500,141,141,45]]</obb>`  
**Geometry-Guided Learning:** The bounding box corresponding to `<obb>[[4500,500,141,141,45]]</obb>` is  
**Response:** `<box>[[400,400,600,600]]</box>`

Figure 3. A demo of PAL and GGL when the sparse signal corresponds to HBB, and the dense signal corresponds to OBB.

**Prompt-Assisted Learning** refers to completing visual grounding with the help of additional prompts, such as predicting the OBB of an object based on its known HBB. This process can be understood as an increase in information entropy and aims to help the model acquire the ability to generate dense signals from sparse ones. Since dense signals contain more information than sparse signals, this process still requires the model to extract additional information from the image to bridge the gap between the signals. PAL can be expressed by the following equation:

$$t_{dense} = \mathcal{F}(\mathbf{I}, \{q, t_{sparse}\}) \quad (2)$$

where  $t_{sparse}$  represents the sparse textualized signal, which can be either Text-HBB or Text-OBB here.  $t_{dense}$  represents the textualized signal that is denser than  $t_{sparse}$ .

**Geometry-Guided Learning** converts dense signals into sparse ones guided by geometric knowledge, reducing information entropy. This means that GGL does not require the image as input; the transformation process can be achieved solely based on geometric knowledge. For example, the HBB that encloses an OBB can be obtained by calculating its four corner points' maximum and minimum values. GGL can be expressed as:

$$t_{sparse} = \mathcal{F}(\{q, t_{dense}\}) \quad (3)$$

where  $t_{dense}$  denotes the dense textualized signal, which can be either Text-OBB or Text-Mask. Fig. 3 presents a demo of PAL and GGL. Similarly to existing VLMs, GeoGround is supervised solely by the text regression loss.

**BBox Consistency Score.** Ideally, the model outputs for the same object should have a similar enclosing bounding box. However, the positions of the HBB, OBB, and mask outputs may differ. To assess prediction consistency, we propose the BBox Consistency Score (BCS):

$$BCS = \frac{1}{3} \left( \text{IoU}(s_{hbb}, f_{obb2hbb}(s_{obb})) + \text{IoU}(s_{hbb}, f_{mask2hbb}(s_{mask})) + \text{IoU}(f_{obb2hbb}(s_{obb}), f_{mask2hbb}(s_{mask})) \right) \quad (4)$$

Dataset	Format	# Refers	GSD (m)	Image Width	3D
RSVG [26]	HBB	5,505	0.24~4.88	1,024	✘
DIOR-RSVG [37]	HBB	27,133	0.5~30	800	✘
GeoChat [9]	OBB	63,883	0.3~0.8	600~1,024	✘
VRSBench [13]	OBB	38,689	0.1~30	512	✘
AVVG (Ours)	OBB	26,465	0.007~0.04	4,000	✔
<b>refGeo (Ours)</b>	<b>Mixed</b>	<b>161,675</b>	<b>0.007~30</b>	<b>512~4,000</b>	<b>✔</b>

Table 1. List of datasets used to create our referring expression instruction set for GeoGround VLM training. To ensure diversity, we include RS visual grounding datasets with varying ground sampling distance (GSD) and sizes.

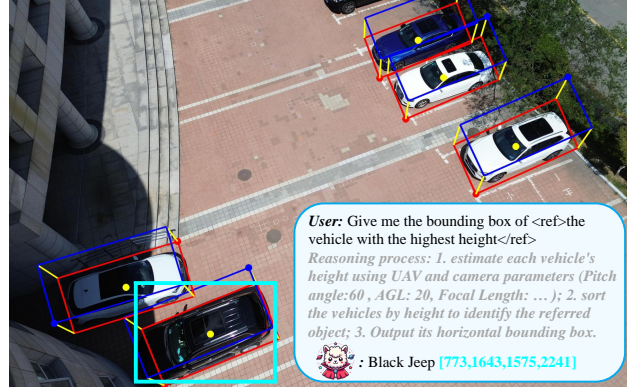


Figure 4. Illustration of the 3D spatial understanding capabilities of the GeoGround model enabled by the AVVG dataset. The 3D bounding boxes are computed using perspective geometry.

where  $s_{hbb}$ ,  $s_{obb}$ , and  $s_{mask}$  represent HBB, OBB, and mask signals, respectively.  $\text{IoU}$  denotes the Intersection over Union.  $f_{obb2hbb}$  and  $f_{mask2hbb}$  represent the functions that compute the enclosing HBB from the OBB and mask, respectively. The BCS ranges from 0 to 1. When the model predictions are completely consistent, the BCS equals 1.

## 4. refGeo

To address the issue of limited generalization capability in VLMs caused by the relatively small size of existing RS visual grounding datasets, we present a large-scale RS referring expression comprehension dataset, refGeo. It integrates most existing RS visual grounding datasets. The details of each dataset are provided in Tab. 1. Since both GeoChat [9] and VRSBench [13] use DIOR [12] image data, which overlap with DIOR-RSVG [37], we remove the samples corresponding to images that appear in the DIOR-RSVG test and validation sets from the GeoChat and VRSBench training set to prevent data leakage.

**Aerial Vehicle Visual Grounding.** Moreover, we propose a new aerial vehicle visual grounding dataset (AVVG) using unmanned aerial vehicles (UAVs), which presents two

Model	DIOR-RSVG-Test	DIOR-RSVG-Val	RSVG-Test	RSVG-Val	GeoChat*	VRSBench*	AVVG	AVG
<i>Specialized Models</i>								
MGVLF [37]	76.78	-	-	-	-	-	-	-
GeoVG [26]	-	-	59.40	58.20	-	-	-	-
<i>Generalist VLMs</i>								
InternVL2-8B [5]	14.42	12.99	0.16	0.67	9.91	5.47	0.34	6.28
InternVL2-40B [5]	15.06	14.87	0.41	0.67	21.13	13.64	8.23	10.57
Qwen-VL [1]	32.22	32.01	2.04	4.66	35.36	31.07	0.31	19.66
Qwen2-VL [28]	44.25	43.32	20.13	19.15	30.92	32.88	17.73	29.77
<i>Remote Sensing VLMs</i>								
GeoChat [9]	24.05	23.35	2.04	3.08	22.74	11.52	0.28	12.44
LHRS-Bot [20]	17.59	17.04	1.56	0.95	3.25	1.19	0.00	5.94
H <sup>2</sup> RSVLM [21]	48.04	-	-	-	-	-	-	-
EarthGPT [39]	76.65	-	-	-	-	-	-	-
<i>Supervised Fine-Tuning on refGeo</i>								
Qwen-VL [1]	58.76	58.65	10.59	12.99	41.75	47.38	9.53	34.24
GeoChat [9]	61.96	60.27	14.67	16.32	56.99	51.36	11.52	39.01
LLaVA-1.5-7B [15]	65.98	64.46	20.95	19.98	63.76	57.17	15.05	43.91
GeoGround (N=32)	76.42	76.18	26.57	26.73	68.65	65.35	21.34	51.61
GeoGround (N=16)	<b>77.73</b>	<b>77.18</b>	<b>26.65</b>	<b>27.64</b>	<b>70.24</b>	<b>66.04</b>	<b>21.58</b>	<b>52.44</b>
Improvement over Runner-up ↑	<b>1.4%</b>	<b>19.7%</b>	<b>27.2%</b>	<b>38.3%</b>	<b>10.2%</b>	<b>15.5%</b>	<b>21.7%</b>	<b>19.4%</b>

Table 2. Performance (Acc@0.5%) comparison on 7 benchmarks. \* indicates that the test set has been modified. The last row indicates the performance improvement of our method compared to the runner-up VLM, further demonstrating the superiority of the GeoGround.

key advantages over previous RS visual grounding datasets.

- 1) **3D Visual Grounding:** This dataset leverages UAVs and camera parameters to map pixel coordinates to the camera coordinate system, extending the conventional 2D plane of RS visual grounding tasks into 3D space for the first time. As shown in Fig. 4, part of referring expressions requires the VLM to have spatial reasoning capabilities to accurately locate the object. This extension provides essential data support for further exploration of spatial intelligence in remote sensing, fostering VLMs to perceive 3D space from 2D images projected from the real world, much like humans do.
- 2) **Fine-Grained Attributes:** Our dataset is also the first aerial vehicle dataset meticulously annotated with vehicle brands and models. Although visual grounding tasks involving fine-grained vehicle attributes are more challenging, they are more aligned with real-world requirements.

**Mask Generation.** To support pixel-level visual grounding tasks, we employ the SAM [8] to generate mask annotations based on existing bounding box annotations. Specifically, we input the bounding box as a prompt along with the image into the SAM-H model, which outputs a mask and its corresponding confidence score. To ensure the quality of the masks, predictions with a confidence score below 0.9 are discarded. In such cases, inspired by SegVG [7], we directly use the bounding box as a mask to provide dense supervision signals. For masks with confidence scores above

0.9, following the idea of RSMIN [16], we apply the morphological dilation algorithm to fix the mask. As a result, we constructed the refGeo dataset, which provides annotations in three forms: HBB, OBB, and segmentation mask.

## 5. Experiments

### 5.1. Implementation Details

Our method is based on LLaVA-1.5-7B [15] with the input image resolution fixed at  $336 \times 336$ . We utilize the AdamW optimizer [18], starting with an initial learning rate of  $2e-4$ , followed by a linear decay schedule after a warm-up phase with a 0.03 ratio. To reduce GPU memory consumption, all models are fine-tuned using LoRA with a rank of 64, in conjunction with ZeRO-2 stage memory optimization. All models are trained on 8 NVIDIA V100 GPUs (32GB) with a global batch size of 128 for 5 epochs. The inference batch size is set to 1 for all experiments. 3 RS object detection datasets [12, 25, 34] are used during the fine-tuning of GeoGround to enhance its basic visual perception capabilities.

### 5.2. Referring Expression Comprehension

**Settings.** We follow standard evaluation protocols [13, 21] and assess the REC task using Acc@0.5 metric. Except for H2RSVLM [21] and EarthGPT [39], whose metrics are cited in the original articles due to the lack of open source code, the results for the other VLMs are obtained by

Method	GeoChat*	VRSBench*	AVVG	AVG
GeoChat w/o ft	31.88	11.54	0.00	14.47
LLaVA-1.5-7B	51.47	43.71	12.56	35.91
GeoGround (N=16)	<b>59.72</b>	<b>53.22</b>	<b>13.93</b>	<b>42.29</b>

Table 3. Performance (Acc@0.5) comparison on 3 REC benchmarks that provide OBB annotations.

Method	Color	Type	Brand	AVG
LLaVA-1.5-7B	1.39	1.29	0.54	1.07
GeoGround (N=16)	<b>9.75</b>	<b>5.60</b>	<b>5.44</b>	<b>6.93</b>

Table 4. Performance (AP@0.5) comparison on the AVVG Generalized REC benchmark.

inference with the official model weights provided. For the GeoChat [9], we convert its output OBBs to HBBs.

**Results.** Tab. 2 compares the performance of GeoGround with 2 specialized models and 8 mainstream VLMs on 7 REC benchmarks. GeoGround achieves the best performance across all benchmarks, surpassing the specialized model on the DIOR-RSVG test set. VLMs fine-tuned on our refGeo dataset, such as Qwen-VL [1] and GeoChat [9], showed significant improvements on the REC task, validating the effectiveness of the scaling law in the field of RS visual grounding. Benefiting from the wide range of image resolutions and GSD in refGeo, the fine-tuned model showed significant performance improvements on datasets with a high proportion of small objects, such as RSVG and AVVG. GeoGround achieves the best performance when the resolution of Text-Mask is set to 16. This could be due to the increased difficulty of training at higher resolutions. Although low resolution leads to coarse masks, they can be seen as attention mechanisms that aid in localizing the approximate object area.

### 5.3. REC with OBB

**Settings.** Following GeoChat [9], we also use Acc@0.5 as metric, with the difference being that rotated IoU [35] is used instead of normal IoU during the calculation.

**Results.** Tab. 3 compares the performance of GeoGround with GeoChat and LLaVA-1.5 on three REC benchmarks that provide OBB annotations. The results demonstrate GeoGround’s dominance in RS visual grounding tasks based on OBB, further validating the effectiveness of our hybrid supervision approach. Due to the increased number of parameters to learn, this task is more challenging than standard REC, resulting in lower scores on the OBB task compared to the HBB task, even on the same test set.

Method	Acc@0.5 (Mask)		mIoU	
	Val	Test	Val	Test
RSMIN [16]	74.66	74.26	65.10	64.20
LISA [10]	27.07	24.51	27.84	26.78
PixelLM [24]	33.46	28.81	33.89	31.65
NExT-Chat [38]	28.97	26.37	26.98	24.98
GeoGround (N=16)	42.93	40.57	42.24	41.05
GeoGround (N=32)	63.25	60.97	56.36	54.92
GeoGround (N=16) + SAM	68.69	<b>67.50</b>	<b>61.10</b>	<b>60.50</b>
GeoGround (N=32) + SAM	<b>68.88</b>	66.06	60.80	58.93

Table 5. Performance comparison of RES task on the RRSIS-D.

Model	VQA	Image Captioning		REC
	Acc	METEOR	ROUGE-L	Acc@0.5
LLaVA-1.5-7B	<b>70.3</b>	<b>34.1</b>	40.7	44.1
GeoGround (N=16)	69.8	33.8	<b>40.8</b>	<b>65.7</b>

Table 6. Performance of visual understanding on VRSBench.

### 5.4. Generalized REC

**Settings.** We present an RS Generalized REC benchmark based on AVVG, which differs from standard REC in that one referring expression may correspond to multiple objects. We adhere to the VOC evaluation protocols [6] and evaluate our methods using the AP@0.5 metric.

**Results.** Tab. 4 compares the performance of GeoGround and LLaVA-1.5 when using color, type, and brand as referring conditions. The results validate the effectiveness of our hybrid supervision approach and indicate that this task is more challenging than standard REC.

### 5.5. Referring Expression Segmentation

**Settings.** We utilize Acc@0.5 and Mean Intersection-over-Union (mIoU) as evaluation metrics, similar to prior studies [32, 36]. As GeoGround is currently the only RS VLM that supports the RES task, we compare it with three generalist VLMs that possess native segmentation capabilities on the RES task in the RRSIS-D dataset [16].

**Results.** Tab. 5 demonstrates that GeoGround exhibits superior performance in the pixel-level RS vision grounding task. Unlike the other VLMs, GeoGround does not require the introduction of an additional mask decoder, as it inherently possesses segmentation capabilities. Moreover, we attempt to use SAM [8] to refine the coarse masks generated by GeoGround, which allowed GeoGround to achieve results that match the performance of the best RS referring segmentation model [16]. See Appendix for more details.

Options	Acc@0.5			BCS
	HBB	OBB→HBB	Mask→HBB	
LLaVA-1.5-7B	79.84	-	-	-
+ Multiple Signals	87.56	80.76	61.40	0.62
+ PAL	86.76	80.82	63.24	0.63
+ GGL	<b>87.87</b>	<b>81.83</b>	<b>64.95</b>	<b>0.64</b>

Table 7. Ablation Study of Hybrid Supervision on RRSIS-D.

HBB→OBB	HBB←OBB	Acc@0.5 (HBB)	Acc@0.5 (OBB)	BCS
⊗	⊗	60.87	58.68	0.67
PAL	⊗	61.37	59.12	0.68
⊗	PAL	60.83	58.27	0.68
⊗	GGL	60.60	58.81	0.69
PAL	PAL	61.18	59.53	0.69
PAL	GGL	<b>61.39</b>	<b>59.71</b>	<b>0.70</b>

Table 8. Influence of signal consistency on DIOR-RSVG.

HBB	OBB	Mask	Acc@0.5 (HBB)		Acc@0.5 (OBB)	
			DIOR-RSVG	RSVG	VRSBench	GeoChat
✓	⊗	⊗	65.98	20.95	41.45	42.95
⊗	✓	⊗	60.75	14.51	43.71	51.47
✓	✓	⊗	68.49	22.66	48.01	55.64
✓	✓	✓	<b>68.61</b>	<b>23.47</b>	<b>49.66</b>	<b>56.43</b>

Table 9. Influence of multiple supervised signals on GeoGround.

## 5.6. Visual Understanding

**Settings.** We utilize Accuracy, METEOR and ROUGE-L as evaluation metrics for VQA and image captioning tasks, similar to prior studies [9, 13].

**Results.** Tab. 6 compares the visual understanding performance of LLaVA-1.5 and GeoGround, both fine-tuned with the VRSBench [13] versatile instruction set. These results indicate that GeoGround’s performance on VQA and image captioning tasks fluctuates slightly compared to LLaVA-1.5, but shows significant improvement in the REC task. This confirms that our approach enhances region-level understanding without compromising the holistic image comprehension capabilities of VLMs.

## 5.7. Ablation Study

**Effect of Hybrid Supervision.** Tab. 7 presents the ablation study of the components in our proposed hybrid supervision method. To compute BCS, we first convert both OBB and mask into HBB before calculating Acc@0.5. The results confirm their effectiveness and further highlight the importance of output consistency in improving performance. Tab. 8 illustrates the impact of different learning strategies on the performance of VLM. All models are trained on the training set and evaluated on the DIOR-RSVG test set. The results show that PAL improves per-

Method	DownSample	Resolution	Length	Acc@0.5
HBB	-	-	-	58.74
Text4Seg [11]	NEAREST	16	330	17.68
Text4Seg [11]	MaxPooling	16	397	43.09
Text-Mask	MaxPooling	16	157	50.73
Text-Mask	MaxPooling	24	237	56.10
Text-Mask	MaxPooling	32	316	<b>57.50</b>

Table 10. Discrepancies between Text-Mask and Text4Seg. Length represents the average length of the model outputs.

Method	Format	Range	Acc@0.5	Acc@0.7
GeoChat	$[x_1, y_1, x_2, x_2, \theta]$	(0, 90)	26.56	8.24
polygon	$[x_1, y_1, \dots, x_4, x_4]$	-	26.93	11.26
oc	$[x_c, y_c, w, h, \theta]$	(0, 90)	31.29	13.61
le90	$[x_c, y_c, w, h, \theta]$	[-90, 90)	<b>35.78</b>	15.43
le135	$[x_c, y_c, w, h, \theta]$	[-45, 135)	35.39	<b>15.56</b>

Table 11. Performance comparison of 5 OBB angle representations on the VRSBench, with IoU computed using OBB.

formance when predicting dense signals from sparse ones, while GM, which requires no visual input, yields better results when predicting sparse signals from dense ones. Tab. 9 further explores the effect of multiple signals on model performance. The results show that direct training with three signals can enhance the visual grounding capability of the VLM on HBB and OBB tasks.

**Design Options of Text-Mask** To our best knowledge, Text4Seg [11] is the only work to attempt to treat masks as text. However, with longer referring expressions, its semantic descriptors become overly redundant. Tab. 10 compares the performance of our proposed Text-Mask with Text4Seg on the DIOR-RSVG test set. The HBB prediction is obtained by calculating the bounding box from the boundary of the segmentation mask. Experiments show that mapping the mask to a binary matrix not only reduces the text length of Text4Seg by 40% but also improves its performance by 18%. Since the objects in RS are relatively small, using the nearest downsampling method leads to the loss of mask information for small objects, resulting in significant performance degradation. While increasing the mask quantization resolution can further improve the segmentation accuracy, longer output text sequences increase the inference time and training difficulty.

**Angle Representation of OBB.** Tab. 11 compares 5 common OBB angle representations in the rotated object detection community [44]. The results indicate that different angle representations affect the visual grounding capability of VLM. Specifically, the angle representation used by GeoChat [9] exhibits poor performance, whereas the two

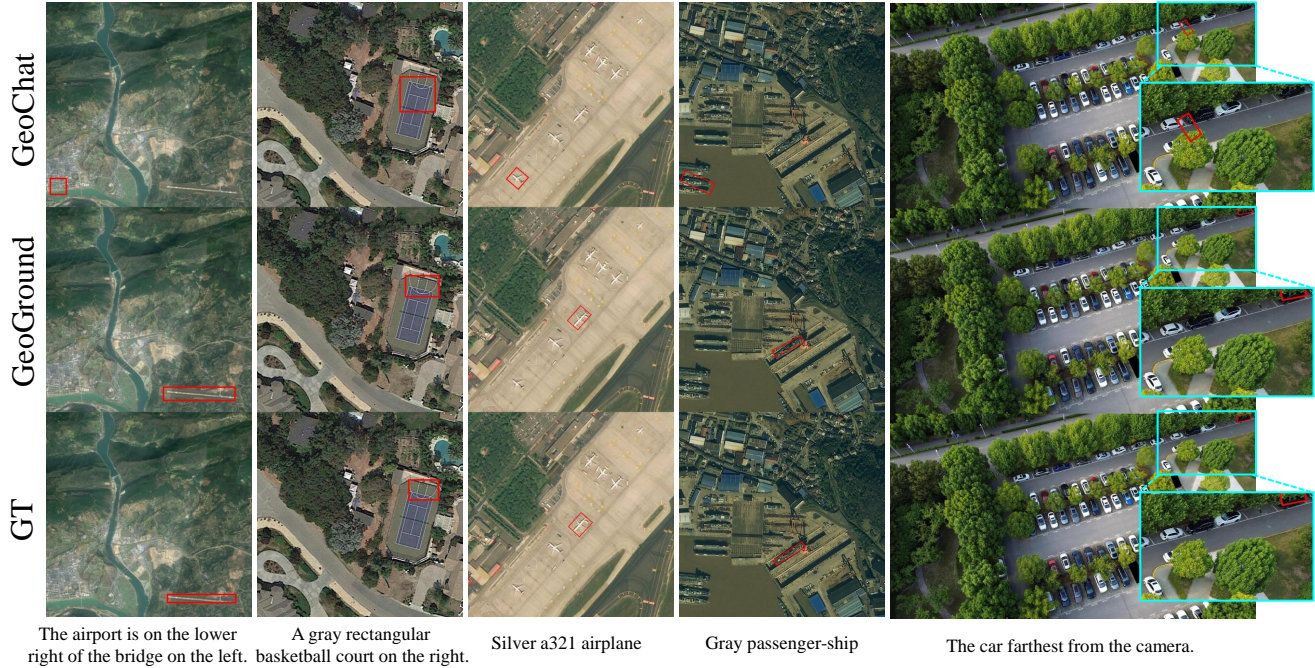


Figure 5. Visualizations of GeoGround and GeoChat on the REC task with HBB and OBB.

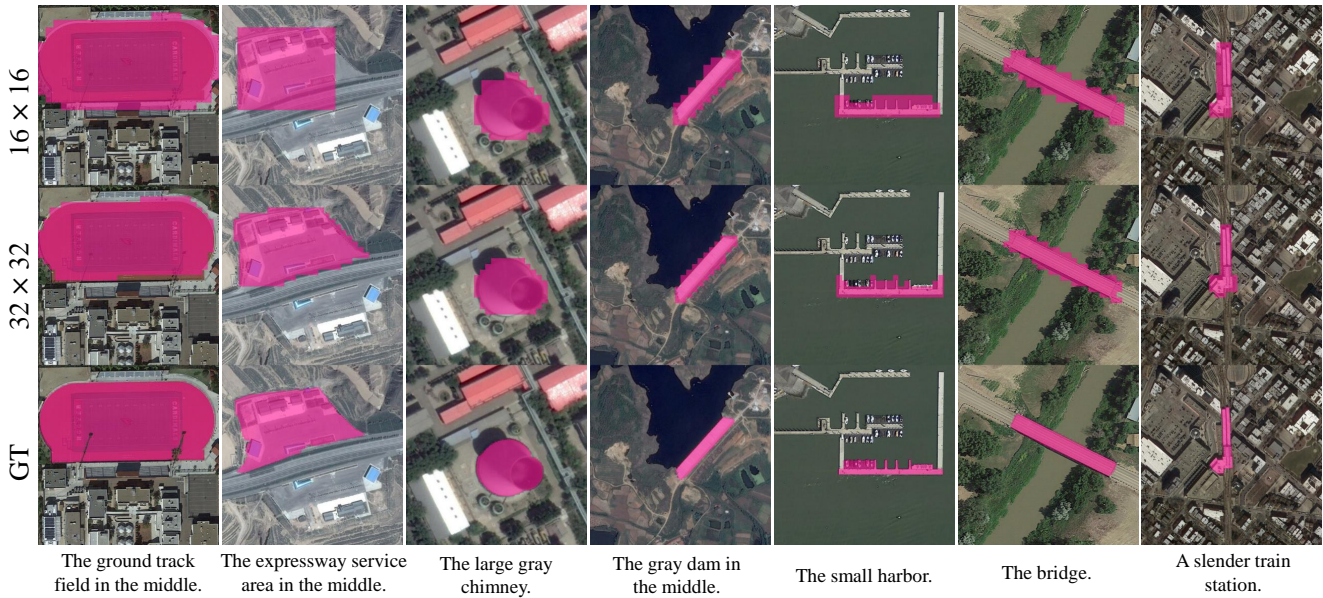


Figure 6. Visualizations of GeoGround with different resolutions of Text-Mask on the RRSIS-D test set.

long-edge representations, le90 and le135, demonstrate superior results. Ultimately, we selected le90 as the default angle representation for GeoGround.

### 5.8. Visualization Examples

Qualitative comparisons between GeoGround and GeoChat are presented in Fig. 5, which includes HBBs and OBBs. It can be observed that GeoGround consistently demonstrates

superior localization accuracy, whether handling simple or relatively complex referential expressions. Additionally, it exhibits 3D spatial understanding, enabling it to infer 3D distances from 2D images. Fig. 6 compares the performance of GeoGround in the RES task under different resolutions of Text-Mask. When the resolution is 32, although the coarse mask edges still exhibit small jaggedness, the result is already very close to the ground truth. These results



fully validate the effectiveness of GeoGround in addressing the pixel-level visual grounding task in RS.

## 6. Conclusion

Although remote sensing (RS) visual grounding tasks using horizontal bounding boxes, oriented bounding boxes, and segmentation masks have progressed, no model has unified these tasks due to framework limitations. To address this, we propose GeoGround, a novel framework that unifies box-level and pixel-level visual grounding tasks in a single model. Instead of adding extra encoders or decoders, GeoGround empowers large vision-language models (VLMs) to perform pixel-level visual grounding by treating the segmentation mask as text using our Text-Mask method. It does not compromise the model’s conversational abilities or its image-level understanding capabilities. We also introduce a large-scale RS visual grounding instruction-following dataset, refGeo, that offers a comprehensive benchmark for various visual grounding tasks of RS and serves as a valuable corpus for RS VLMs. Our comprehensive benchmarks and ablation studies provide important insights for the development of VLMs in the RS domain.

## References

- [1] Jinze Bai, Shuai Bai, Shusheng Yang, Shijie Wang, Sinan Tan, Peng Wang, Junyang Lin, Chang Zhou, and Jingren Zhou. Qwen-vl: A frontier large vision-language model with versatile abilities. *arXiv preprint arXiv:2308.12966*, 2023. [2](#), [5](#), [6](#), [1](#)
- [2] Jun Chen, Deyao Zhu, Xiaoqian Shen, Xiang Li, Zechun Liu, Pengchuan Zhang, Raghuraman Krishnamoorthi, Vikas Chandra, Yunyang Xiong, and Mohamed Elhoseiny. Minigt-v2: large language model as a unified interface for vision-language multi-task learning. *arXiv preprint arXiv:2310.09478*, 2023. [2](#)
- [3] Keqin Chen, Zhao Zhang, Weili Zeng, Richong Zhang, Feng Zhu, and Rui Zhao. Shikra: Unleashing multimodal llm’s referential dialogue magic. *arXiv preprint arXiv:2306.15195*, 2023. [2](#), [3](#), [1](#)
- [4] Ting Chen, Saurabh Saxena, Lala Li, David J Fleet, and Geoffrey Hinton. Pix2seq: A language modeling framework for object detection. *arXiv preprint arXiv:2109.10852*, 2021. [2](#)
- [5] Zhe Chen, Jiannan Wu, Wenhai Wang, Weijie Su, Guo Chen, Sen Xing, Muyan Zhong, Qinglong Zhang, Xizhou Zhu, Lewei Lu, Bin Li, Ping Luo, Tong Lu, Yu Qiao, and Jifeng Dai. Internvl: Scaling up vision foundation models and aligning for generic visual-linguistic tasks. *arXiv preprint arXiv:2312.14238*, 2023. [2](#), [5](#), [1](#), [3](#)
- [6] Mark Everingham, Luc Van Gool, Christopher KI Williams, John Winn, and Andrew Zisserman. The pascal visual object classes (voc) challenge. *International journal of computer vision*, 88:303–338, 2010. [6](#)
- [7] Weitai Kang, Gaowen Liu, Mubarak Shah, and Yan Yan. Segvg: Transferring object bounding box to segmentation for visual grounding. In *European Conference on Computer Vision*, pages 57–75. Springer, 2025. [5](#)
- [8] Alexander Kirillov, Eric Mintun, Nikhila Ravi, Hanzi Mao, Chloe Rolland, Laura Gustafson, Tete Xiao, Spencer Whitehead, Alexander C Berg, Wan-Yen Lo, et al. Segment anything. In *Proceedings of the IEEE/CVF International Conference on Computer Vision*, pages 4015–4026, 2023. [2](#), [5](#), [6](#)
- [9] Kartik Kuckreja, Muhammad Sohail Danish, Muzammal Naseer, Abhijit Das, Salman Khan, and Fahad Shahbaz Khan. Geochat: Grounded large vision-language model for remote sensing. In *Proceedings of the IEEE/CVF Conference on Computer Vision and Pattern Recognition*, pages 27831–27840, 2024. [1](#), [2](#), [4](#), [5](#), [6](#), [7](#), [3](#)
- [10] Xin Lai, Zhuotao Tian, Yukang Chen, Yanwei Li, Yuhui Yuan, Shu Liu, and Jiaya Jia. Lisa: Reasoning segmentation via large language model. In *Proceedings of the IEEE/CVF Conference on Computer Vision and Pattern Recognition*, pages 9579–9589, 2024. [2](#), [6](#)
- [11] Mengcheng Lan, Chaofeng Chen, Yue Zhou, Jiaxing Xu, Yiping Ke, Xinjiang Wang, Litong Feng, and Wayne Zhang. Text4seg: Reimagining image segmentation as text generation. *arXiv preprint arXiv:2410.09855*, 2024. [3](#), [7](#), [1](#)
- [12] Ke Li, Gang Wan, Gong Cheng, Liqiu Meng, and Junwei Han. Object detection in optical remote sensing images: A survey and a new benchmark. *ISPRS journal of photogrammetry and remote sensing*, 159:296–307, 2020. [1](#), [4](#), [5](#), [2](#)
- [13] Xiang Li, Jian Ding, and Mohamed Elhoseiny. Vrsbench: A versatile vision-language benchmark dataset for remote sensing image understanding. *arXiv preprint arXiv:2406.12384*, 2024. [2](#), [4](#), [5](#), [7](#)
- [14] Yunpeng Li, Xiangrong Zhang, Jing Gu, Chen Li, Xin Wang, Xu Tang, and Licheng Jiao. Recurrent attention and semantic gate for remote sensing image captioning. *IEEE Transactions on Geoscience and Remote Sensing*, 60:1–16, 2021. [2](#)
- [15] Haotian Liu, Chunyuan Li, Qingyang Wu, and Yong Jae Lee. Visual instruction tuning. *arXiv preprint arXiv:2304.08485*, 2023. [2](#), [5](#)
- [16] Sihan Liu, Yiwei Ma, Xiaoqing Zhang, Haowei Wang, Jiayi Ji, Xiaoshuai Sun, and Rongrong Ji. Rotated multi-scale interaction network for referring remote sensing image segmentation. In *Proceedings of the IEEE/CVF Conference on Computer Vision and Pattern Recognition*, pages 26658–26668, 2024. [1](#), [2](#), [5](#), [6](#)
- [17] Sylvain Lobry, Diego Marcos, Jesse Murray, and Devis Tuia. Rsvqa: Visual question answering for remote sensing data. *IEEE Transactions on Geoscience and Remote Sensing*, 58(12):8555–8566, 2020. [2](#)
- [18] I Loshchilov. Decoupled weight decay regularization. *arXiv preprint arXiv:1711.05101*, 2017. [5](#)
- [19] Georgii Mikriukov, Mahdyar Ravanbakhsh, and Begüm Demir. Deep unsupervised contrastive hashing for large-scale cross-modal text-image retrieval in remote sensing. *arXiv preprint arXiv:2201.08125*, 2022. [2](#)
- [20] Dilxat Muhtar, Zhenshi Li, Feng Gu, Xueliang Zhang, and Pengfeng Xiao. Lhrs-bot: Empowering remote sensing

- with vgi-enhanced large multimodal language model. *arXiv preprint arXiv:2402.02544*, 2024. 2, 5
- [21] Chao Pang, Jiang Wu, Jiayu Li, Yi Liu, Jiaying Sun, Weijia Li, Xingxing Weng, Shuai Wang, Litong Feng, Gui-Song Xia, et al. H2rsvlm: Towards helpful and honest remote sensing large vision language model. *arXiv preprint arXiv:2403.20213*, 2024. 2, 5
- [22] Zhiliang Peng, Wenhui Wang, Li Dong, Yaru Hao, Shaohan Huang, Shuming Ma, and Furu Wei. Kosmos-2: Grounding multimodal large language models to the world. *arXiv preprint arXiv:2306.14824*, 2023. 2, 1
- [23] Alec Radford, Jong Wook Kim, Chris Hallacy, Aditya Ramesh, Gabriel Goh, Sandhini Agarwal, Girish Sastry, Amanda Askell, Pamela Mishkin, Jack Clark, et al. Learning transferable visual models from natural language supervision. In *International conference on machine learning*, pages 8748–8763. PMLR, 2021. 2
- [24] Zhongwei Ren, Zhicheng Huang, Yunchao Wei, Yao Zhao, Dongmei Fu, Jiashi Feng, and Xiaojie Jin. Pixellm: Pixel reasoning with large multimodal model. In *Proceedings of the IEEE/CVF Conference on Computer Vision and Pattern Recognition*, pages 26374–26383, 2024. 6
- [25] Xian Sun, Peijin Wang, Zhiyuan Yan, Feng Xu, Ruiping Wang, Wenhui Diao, Jin Chen, Jihao Li, Yingchao Feng, Tao Xu, et al. Fair1m: A benchmark dataset for fine-grained object recognition in high-resolution remote sensing imagery. *ISPRS Journal of Photogrammetry and Remote Sensing*, 184:116–130, 2022. 1, 5, 4
- [26] Yuxi Sun, Shanshan Feng, Xutao Li, Yunming Ye, Jian Kang, and Xu Huang. Visual grounding in remote sensing images. In *Proceedings of the 30th ACM International Conference on Multimedia*, pages 404–412, 2022. 1, 2, 4, 5
- [27] Michele Volpi and Devis Tuia. Deep multi-task learning for a geographically-regularized semantic segmentation of aerial images. *ISPRS journal of photogrammetry and remote sensing*, 144:48–60, 2018. 1
- [28] Peng Wang, Shuai Bai, Sinan Tan, Shijie Wang, Zhihao Fan, Jinze Bai, Keqin Chen, Xuejing Liu, Jialin Wang, Wenbin Ge, et al. Qwen2-vl: Enhancing vision-language model’s perception of the world at any resolution. *arXiv preprint arXiv:2409.12191*, 2024. 5, 3
- [29] Sheng Wang, Wei Han, Xiaohui Huang, Xiaohan Zhang, Lizhe Wang, and Jun Li. Trustworthy remote sensing interpretation: Concepts, technologies, and applications. *ISPRS Journal of Photogrammetry and Remote Sensing*, 209:150–172, 2024. 1
- [30] Wenhui Wang, Zhe Chen, Xiaokang Chen, Jiannan Wu, Xizhou Zhu, Gang Zeng, Ping Luo, Tong Lu, Jie Zhou, Yu Qiao, et al. Visionllm: Large language model is also an open-ended decoder for vision-centric tasks. *Advances in Neural Information Processing Systems*, 36, 2024. 2
- [31] Zhecheng Wang, Rajanie Prabha, Tianyuan Huang, Jiajun Wu, and Ram Rajagopal. Skyscript: A large and semantically diverse vision-language dataset for remote sensing. In *Proceedings of the AAAI Conference on Artificial Intelligence*, pages 5805–5813, 2024. 2
- [32] Chenyun Wu, Zhe Lin, Scott Cohen, Trung Bui, and Subhansu Maji. Phrasecut: Language-based image segmentation in the wild. In *Proceedings of the IEEE/CVF Conference on Computer Vision and Pattern Recognition*, pages 10216–10225, 2020. 6
- [33] Jiannan Wu, Muyan Zhong, Sen Xing, Zeqiang Lai, Zhaoyang Liu, Wenhui Wang, Zhe Chen, Xizhou Zhu, Lewei Lu, Tong Lu, et al. Visionllm v2: An end-to-end generalist multimodal large language model for hundreds of vision-language tasks. *arXiv preprint arXiv:2406.08394*, 2024. 2
- [34] Gui-Song Xia, Xiang Bai, Jian Ding, Zhen Zhu, Serge Belongie, Jiebo Luo, Mihai Datcu, Marcello Pelillo, and Liangpei Zhang. Dota: A large-scale dataset for object detection in aerial images. In *Proceedings of the IEEE conference on computer vision and pattern recognition*, pages 3974–3983, 2018. 1, 5, 2, 4
- [35] Xue Yang, Gefan Zhang, Xiaojiang Yang, Yue Zhou, Wentao Wang, Jin Tang, Tao He, and Junchi Yan. Detecting rotated objects as gaussian distributions and its 3-d generalization. *IEEE Transactions on Pattern Analysis and Machine Intelligence*, 45(4):4335–4354, 2022. 6
- [36] Zhenghang Yuan, Lichao Mou, Yuansheng Hua, and Xiao Xiang Zhu. Rrsis: Referring remote sensing image segmentation. *IEEE Transactions on Geoscience and Remote Sensing*, 2024. 1, 2, 6
- [37] Yang Zhan, Zhitong Xiong, and Yuan Yuan. Rsvg: Exploring data and models for visual grounding on remote sensing data. *IEEE Transactions on Geoscience and Remote Sensing*, 61: 1–13, 2023. 1, 2, 4, 5
- [38] Ao Zhang, Liming Zhao, Chen-Wei Xie, Yun Zheng, Wei Ji, and Tat-Seng Chua. Next-chat: An lmm for chat, detection and segmentation. *arXiv preprint arXiv:2311.04498*, 2023. 2, 6
- [39] Wei Zhang, Miaoxin Cai, Tong Zhang, Yin Zhuang, and Xuerui Mao. Earthgpt: A universal multi-modal large language model for multi-sensor image comprehension in remote sensing domain. *IEEE Transactions on Geoscience and Remote Sensing*, 2024. 2, 5, 1
- [40] Zhengyuan Zhang, Wenkai Zhang, Menglong Yan, Xin Gao, Kun Fu, and Xian Sun. Global visual feature and linguistic state guided attention for remote sensing image captioning. *IEEE Transactions on Geoscience and Remote Sensing*, 60: 1–16, 2021. 2
- [41] Zilun Zhang, Tiancheng Zhao, Yulong Guo, and Jianwei Yin. Rs5m and georsclip: A large scale vision-language dataset and a large vision-language model for remote sensing. *IEEE Transactions on Geoscience and Remote Sensing*, 2024. 2
- [42] Yuze Zhao, Jintao Huang, Jinghan Hu, Daoze Zhang, Zeyinzi Jiang, Zhikai Wu, Baole Ai, Ang Wang, Wenmeng Zhou, and Yingda Chen. Swift: A scalable lightweight infrastructure for fine-tuning. *arXiv preprint arXiv:2408.05517*, 2024. 3
- [43] Lianmin Zheng, Wei-Lin Chiang, Ying Sheng, Siyuan Zhuang, Zhanghao Wu, Yonghao Zhuang, Zi Lin, Zhuohan Li, Dacheng Li, Eric Xing, et al. Judging llm-as-a-judge with mt-bench and chatbot arena. *Advances in Neural Information Processing Systems*, 36:46595–46623, 2023. 2
- [44] Yue Zhou, Xue Yang, Gefan Zhang, Jiabao Wang, Yanyi Liu, Liping Hou, Xue Jiang, Xingzhao Liu, Junchi Yan, Chengqi

Lyu, et al. Mmrotate: A rotated object detection benchmark using pytorch. In *Proceedings of the 30th ACM International Conference on Multimedia*, pages 7331–7334, 2022. [3](#), [7](#)

# GeoGround : A Unified Large Vision-Language Model for Remote Sensing Visual Grounding

## Supplementary Material

### 1. Additional Visual Grounding Signal Details

#### 1.1. Type of Signals used in VLMs.

Tab. 12 summarizes several visual grounding signals currently employed in the VLM domain, all of which use the signal textualization paradigm to convert visual grounding tasks into text generation tasks. To the best of our knowledge, we are the first to convert masks of RS objects into text sequences successfully.

Model	Signal	Density	Resolution	Text Length
Kosmos-2 [22]	HBB	Sparse	1/32	2 tokens
Shikra [3]	HBB	Sparse	1/1000	4 numbers
GeoChat [9]	OBB	Medium	1/100	5 numbers
EarthGPT [39]	Polygon	Medium	1/100	8 numbers
Text4Seg [11]	Mask	Dense	1/N	N×N phases
GeoGround	Mask	Dense	1/N	N×N numbers

Table 12. Comparison of different signals used in VLMs.

#### 1.2. Format of HBB Signals.

Tab. 13 presents the numerical ranges and representation precision of several common HBB encoding formats in current grounded VLMs. Additionally, we calculated the number of tokens required by the LLaVA tokenizer to encode a single object using these formats. Format #1, adopted by GeoChat [9], requires more tokens than #2 for the same precision. Since the tokenizer requires more tokens to encode decimal values, Format #3, which normalizes coordinates to 1 and retains three decimal places, results in the highest token count. We recommend using #4 or #5, corresponding to the InternVL [5] and Qwen-VL [1] formats, respectively, as they offer greater precision while requiring fewer tokens. Reducing the number of tokens needed to encode a single object not only lowers the training cost for VLMs but also accelerates inference. Ultimately, we selected #4 as the default HBB format for GeoGround.

#	Range	Precision	Format	#Token
1	[0,100)	100	$\{<x_1><y_1><x_2><y_2>\}$	12~20
2	[0, 100)	100	$[x_1, y_1, x_2, y_2]$	10~14
3	[0,1)	1000	$[x_1, y_1, x_2, y_2]$	18~26
4	[0, 1000)	1000	$[x_1, y_1, x_2, y_2]$	10~18
5	[0, 1000)	1000	$(x_1, y_1), (x_2, y_2)$	10~18

Table 13. Token counts required for encoding several HBB formats using LLaVA model’s tokenizer.

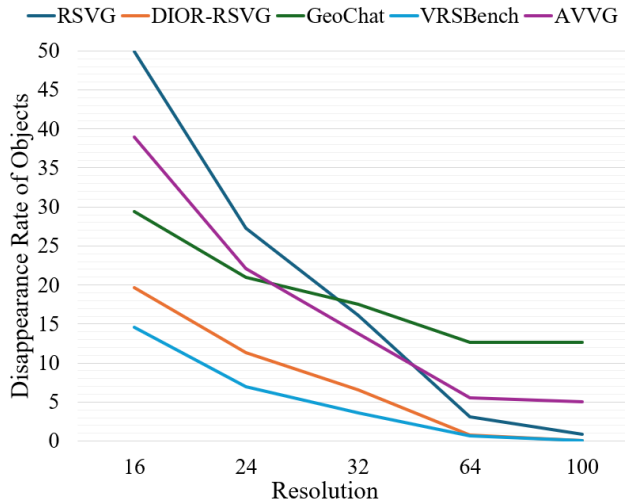


Figure 7. Disappearance rate of objects in masks after resizing to N×N dimensions. The higher the proportion of small objects in the dataset, the greater the disappearance rate.

#### 1.3. Resolution of Signals.

Fig. 7 compares the disappearance rates of objects across 5 remote sensing visual grounding datasets when different quantization resolutions are applied. It can be observed that the datasets, ranked by the proportion of small targets from highest to lowest at a quantization resolution of 16, are RSVG, AVVG, GeoChat, DIOR-RSVG, and VRSBench. This also explains why the VLM scores are relatively low on the RSVG and AVVG datasets. When the quantization resolution is set to 32, the object disappearance rate remains below 20% for all datasets. Thus, Matrix4Seg achieves satisfactory performance when the resolution is set to 32. At a quantization resolution of 100, GeoChat still has a disappearance rate of 12.65%, indicating the presence of some very small targets in the GeoChat dataset.

### 2. Additional Data Details

#### 2.1. Mask Generation.

The released refGeo dataset contains manually annotated HBBs or OBBs. However, the masks used in the experiments are generated through an automated method, and thus their quality cannot be fully guaranteed. Although we set a score threshold, errors in the masks still occur. Interestingly, despite the noise in these mask data, they still

validate the effectiveness of the hybrid supervision training proposed in this paper. In future work, we plan to manually refine these automatically generated masks in refGeo to provide more accurate referring expression segmentation samples for training.

## 2.2. Creation of AVVG.

Existing open-source RS datasets [12, 34] often lack sensor metadata and provide limited target attributes. Consequently, these datasets can only support the formulation of simple visual grounding problems, such as locating an object in the upper-left corner of an image. To develop a spatially aware remote sensing dataset, we use unmanned aerial vehicles to collect data from scratch. This approach ensures comprehensive access to sensor parameters, allowing inversion of the three-dimensional coordinates of image targets based on imaging geometry principles. Data collection is divided into two parts: aerial imagery and ground video.

**Aerial Imagery.** All aerial images in AVVG are collected with a small UAV platform, DJI Mini3, between 10-16 September 2023, in Shanghai. The dataset consists of 4K high-resolution RS images from 11 distinct scenes, captured at 9 different above-ground levels and 3 pitch angles. This implies that these RS images possess different spatial resolutions and perspectives. In addition, the collected images cover a variety of weather scenarios, such as sunny, cloudy, and rainy days, along with different lighting conditions.

**Ground Video.** We record ground videos from the same areas to facilitate accurate annotation of vehicle brands and models. Specifically, we select time slots with relatively low vehicular mobility, avoiding rush hours and meal times. Additionally, to mitigate the vehicle mismatch between drone images and ground videos caused by vehicle entry and exit, we capture two sets of ground videos before and after the drone captures aerial photos. This ensures that vehicles entering or exiting the scene halfway through the capture are recorded in the videos. However, there are instances where vehicles pass through the scene briefly, leading to cases where they are not captured in either video. In such situations, we mask these vehicles with a black mask in the images to ensure that all visible vehicles have fully known attributes. Due to privacy concerns, ground videos will not be released.

**Derivation of Coordinate System Transformation.** The transformation between the pixel coordinate system and the image coordinate system can be represented by an affine



Figure 8. Illustration of the 3D bounding box are obtained by Coordinate System Transformation.

matrix, as follows:

$$\begin{bmatrix} x_P \\ y_P \\ 1 \end{bmatrix} = \begin{bmatrix} \frac{1}{p} & 0 & \frac{w}{2} \\ 0 & \frac{1}{p} & \frac{h}{2} \\ 0 & 0 & 1 \end{bmatrix} \begin{bmatrix} x_I \\ y_I \\ 1 \end{bmatrix} \quad (5)$$

where  $p$  represents the pixel size of the sensor.  $\frac{w}{2}$  and  $\frac{h}{2}$  denote the origin offsets, with the origin of the image coordinate system typically located at the image’s top-left corner. Given the pixel coordinates of a certain point, its corresponding image coordinates can be calculated as follows:

$$\begin{cases} x_I = (x_P - w/2) \cdot p \\ y_I = (y_P - h/2) \cdot p \end{cases} \quad (6)$$

The transformation from the camera coordinate system to the image coordinate system is a conversion from three-dimensional to two-dimensional coordinates. Assuming the focal length of the camera is  $f$ , then we have

$$z_C \begin{bmatrix} x_I \\ y_I \\ 1 \end{bmatrix} = \begin{bmatrix} f & 0 & 0 & 0 \\ 0 & f & 0 & 0 \\ 0 & 0 & 1 & 0 \end{bmatrix} \begin{bmatrix} x_C \\ y_C \\ z_C \\ 1 \end{bmatrix} \quad (7)$$

where  $z_C$  denotes the depth of the point, which can be obtained by a depth camera (binocular or structured light). Because the drone camera we are using cannot provide depth information, we need to find another way.

When the ground satisfies the ground plane assumption, given the AGL of the drone and the pitch angle of the camera, the ground plane equation in the camera coordinate system is as follows:

$$-\cos\theta \cdot Y_C - \sin\theta \cdot Z_C + H = 0 \quad (8)$$

The equation of the line connecting the camera origin to the projection point on the pixel plane in the camera coordinate system is given by:

$$\begin{cases} X_C = x_I \cdot t \\ Y_C = y_I \cdot t \\ Z_C = f \cdot t \end{cases} \quad (9)$$

Substituting the line equation into the ground plane equation yields:

$$t = \frac{H}{y_I \cos\theta + f \sin\theta} \quad (10)$$

Substituting  $t$  back into the line equation yields:

$$\left( \frac{x_I H}{y_I \cos\theta + f \sin\theta}, \frac{y_I H}{y_I \cos\theta + f \sin\theta}, \frac{f H}{y_I \cos\theta + f \sin\theta} \right) \quad (11)$$

Fig. 8 visualizes the 3D bounding box of a vehicle. The implementation process is as follows: First, the 3D coordinates of the vehicle’s center point are calculated in the camera coordinate system. Then, based on the orientation information and the vehicle’s length, width, and height, the 3D coordinates of its eight corner points are computed. Finally, these points in the 3D coordinate system are projected back into the 2D-pixel coordinate system. The visualization results further validate the correctness of this coordinate transformation. With the 3D bounding box of each vehicle available, we can formulate visual grounding problems that require the model to have spatial reasoning abilities to solve. For example, which vehicle is the farthest from the camera? Which vehicle has the highest height?

To preserve the spatial mapping between camera coordinates and pixel coordinates, we refrained from cropping the 4K images to increase the dataset size, as is commonly done in most remote sensing datasets. Since the problems involve fine-grained attributes of the vehicles, we used the HBB coordinates of the object as the answers to these spatial grounding tasks, rather than the 3D bounding box, to control the difficulty and prevent the tasks from becoming excessively challenging.

**Generalized REC Benchmark.** The generalized referring expression comprehension benchmark built using AVVG includes AP@0.5 scores for three fine-grained vehicle attributes. The specific categories for each attribute

	Param Name	Value
Optimizer	Type	AdamW
	Learning rate	2e-4
	Weight decay	0.0
	$(\beta_1, \beta_2)$	(0.9, 0.95)
	Gradient norm clip	1.0
	Scheduler	Linearly decay
	Warmup ratio	0.03
LoRA	Rank	64
	Alpha ( $\alpha$ )	16
	Dropout	0.05
	Module	Linear layers of connector and LLMs
Training	Trainable #Params.	About 2% of the LLM (7B $\rightarrow$ 160M)
	Numerical precision	FP16
	Global batch size	128
	Total epochs	5
	GPUs	V100(32G) $\times$ 8

Table 14. Hyper-parameters and training settings for GeoGround.

are listed as follows: **Color (13)**: golden, brown, orange, silver, gray, blue, white, red, black, pink, green, yellow, purple. **Type (10)**: compact, suv, mid-size, subcompact, mpv, sports, full-size, crossover, sedan, micro-size. **Brand (52)**: skoda, buick, audi, toyota, tesla, volkswagen, mercedes-benz, nio, chevrolet, mazda, hyundai, lexus, honda, bmw, ora, geely, byd, jeep, volvo, renault, roewe, ford, nissan, infiniti, peugeot, cadillac, rising, aito, xpeng, haval, lynk&co, mini, citroen, riich, leap, wey, ideal, changan, harvard, denza, chery, kia, porsche, mg, beijing, smart, baojun, aion, wuling, vgv, hongqi, lexus, lincoln.

### 3. Additional Implementation Details

We employ the LLaVA framework to train LLaVA-1.5 and GeoChat, while the SWIFT [42] framework is used to train the Qwen-VL model. The main experiments cover 3 types of connectors, including MLP (LLaVA-1.5, GeoChat), Pixel Shuffle + MLP (InternVL2) and Cross-attention (Qwen-VL). In addition, the selected VLMs have different input image resolutions: fixed  $336 \times 336$  for LLaVA-1.5, fixed  $448 \times 448$  for Qwen-VL, fixed  $504 \times 504$  for GeoChat, and dynamic input resolution for InternVL2 and Qwen2-VL.

#### 3.1. Details of Training Hyper-parameters.

Tab. 14 presents the training hyperparameters used to train the GeoGround. We adhere primarily to the same settings as GeoChat [9], and these parameters are also consistently applied in other fine-tuned VLMs in this paper. However, we observed that two novel VLMs that support dynamic resolution images, InternVL2 [5] and Qwen2-VL [28], struggled to achieve satisfactory fine-tuning results with the same set of parameters. Unfortunately, we have not yet identified satisfactory training parameters for them.

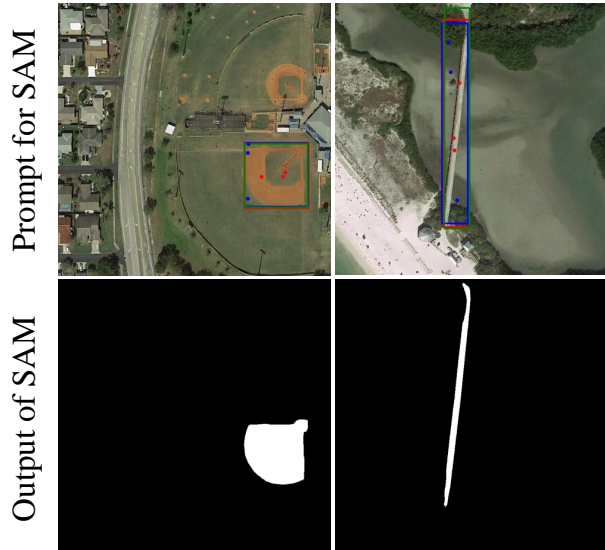


Figure 9. Illustration of the process of refining masks using the SAM. The red and blue dots represent the sampled positive and negative data points. The red, blue, and green bounding boxes represent the ground truth (GT), the GeoGround prediction, and the bounding box of the mask output by SAM, respectively.

### 3.2. Details of Object Detection Training Samples.

We construct a fine-grained vehicle object detection benchmark leveraging the metadata from the test split of our proposed AVVG dataset. Additionally, to assess performance on remote sensing object detection, we create a dataset consisting of 200k samples by combining data from DOTA [34], DIOR [12], FAIR1M [25], and the train split of AVVG. Specifically, we first cropped the original images from the FAIR1M and DOTA datasets into  $512 \times 512$  patches, while retaining the original image sizes for the DIOR and AVVG datasets. We then used the object detection annotations from these datasets to generate training samples, where queries were formulated based on the categories present in each image. Specifically, if an image contains objects from three categories, we constructed three image-text sample pairs accordingly. These data are used to enhance GeoGround’s basic visual perception capabilities.

### 3.3. Implementation of Mask Refiner.

Due to resolution limitations, the proposed Matrix4Seg currently struggles to segment particularly small targets. To address this issue, we can simply refine the output masks using SAM to obtain more accurate masks. Specifically, we resize the binary matrix output from the model to match the dimensions of the image, generating a coarse mask. We then sample 3 positive points and 3 negative points from the mask. The sampling region for the positive points is the intersection between the coarse mask and the predicted HBB, while the sampling region for the negative points is

DIOR-RSVG	RSVG	GeoChat	VRSBench	AVVG	Acc@0.5
✓	✗	✗	✗	✗	58.74
✓	✓	✗	✗	✗	59.84
✓	✓	✓	✗	✗	63.34
✓	✓	✓	✓	✗	65.91
✓	✓	✓	✓	✓	<b>65.98</b>

Table 15. Influence of varying training sample sizes on the LLaVA model’s REC performance on DIOR-RSVG test set.

DIOR	DOTA	FAIR1M	AVVG	Acc@0.5
✗	✗	✗	✗	58.74
✓	✗	✗	✗	59.70
✓	✓	✗	✗	72.61
✓	✓	✓	✗	<b>73.59</b>
✓	✓	✓	✓	73.43

Table 16. Influence of varying object detection sample sizes on the LLaVA model’s REC performance for the DIOR-RSVG test set.

AVVG	DIOR	DOTA	FAIR1M	Overall AP@0.5
✓	✗	✗	✗	1.04
✓	✓	✗	✗	3.11
✓	✓	✓	✗	4.05
✓	✓	✓	✓	<b>4.95</b>

Table 17. Influence of varying training sample sizes on the LLaVA model’s Generalized REC performance for the AVVG test set.

the difference between the coarse mask and the predicted HBB. Subsequently, the positive and negative points, along with the predicted HBB, are used as prompts and input into SAM. If no positive or negative sample points are available, only the predicted HBB is used as the prompt for SAM. Since SAM is training-free, it can be regarded as a post-processing method. As shown in Tab. 5, the precision of the masks can be further improved after refinement.

### 3.4. Visual Instruction Templates

Fig. 10 lists all the instruction templates used during the training of GeoGround. During training, a query is randomly selected from a set of five for each iteration.

## 4. Additional Quantitative Results

### 4.1. More Results on REC.

Tab. 15 shows that as more supervised fine-tuning samples are added to the training set, the Acc@0.5 metric, computed using HBBs on the DIOR-RSVG test set, exhibits a continuous upward trend for the LLaVA-1.5-7B model. This indicates that the scaling law remains effective, suggesting that further increasing the number of visual grounding samples in the RS domain is still a promising avenue.

Furthermore, we conducted an in-depth investigation

into the impact of object detection on the REC task. As shown in Tab. 16, incorporating object detection samples during training can also improve the REC performance of the model. An interesting observation is that, although DIOR-RSVG is constructed using images from the DIOR dataset for the visual grounding task, incorporating object detection samples from the DIOR dataset only improves the results by approximately 1%. However, when object detection samples from the DOTA dataset are added, whose images come from a different source, the performance increases by more than 10%. This indicates that the improvement in the performance of the REC task through object detection is not only due to data leakage. Since the AVVG data set is designed for fine-grained vehicle attribute detection and only contains vehicles as target objects, it does not contribute to the performance improvement in the DIOR-RSVG data set.

#### **4.2. More Results on Generalized REC.**

Tab. 17 shows that adding Generalized REC training samples based on other object detection datasets can also improve the model’s performance on AVVG.

### **5. Additional Qualitative Results**

See more qualitative results of the REC task in Figs. 11 and 12. See more qualitative results of the REC with OBB task in Figs. 13, 14 and 15. See more qualitative results of the RES task in Figs. 16, 17, 18, 19 and 20.



**Query for REC:**

[refer] give me the bounding box of <ref>{prompt}</ref>

[refer] output the bounding box of the <ref>{prompt}</ref> in the image.

[refer] from this image, provide the bounding box for <ref>{prompt}</ref>.

[refer] please provide the bounding box coordinate of the region this sentence describes: <ref>{prompt}</ref>

[refer] can you locate and provide the bounding box for <ref>{prompt}</ref> in the given image?

**Response:** <box>{hbb}</box>

**Query for REC with OBB:**

[refer] give me the oriented bounding box of <ref>{prompt}</ref>

[refer] output the oriented bounding box of the <ref>{prompt}</ref> in the image.

[refer] from this image, provide the oriented bounding box for <ref>{prompt}</ref>.

[refer] please provide the oriented bounding box coordinate of the region this sentence describes: <ref>{prompt}</ref>

[refer] can you locate and provide the oriented bounding box for <ref>{prompt}</ref> in the given image?

**Response:** <obb>{obb}</obb>

**Query for RES:**

[refer] give me the segmentation mask of <ref>{prompt}</ref>

[refer] output the segmentation mask of the <ref>{prompt}</ref> in the image.

[refer] from this image, provide the segmentation mask for <ref>{prompt}</ref>.

[refer] please provide the segmentation mask of the region this sentence describes: <ref>{prompt}</ref>.

[refer] can you segment the <ref>{prompt}</ref> in the given image?

**Response:** <seg>{mask}</seg>

**Query for Object Detection:**

[refer] give me the bounding box of all <ref>{prompt}</ref>

[refer] output the bounding box of all <ref>{prompt}</ref> in the image.

[refer] from this image, provide the bounding box for all <ref>{prompt}</ref>.

[refer] please provide the bounding box coordinate of all objects in this sentence describes: <ref>{prompt}</ref>

[refer] can you locate and provide the bounding box for all <ref>{prompt}</ref> in the given image?

**Response:** <box>{hbb}</box>

**Query for PAL:**

[refer] give me the dense signal of <ref>{prompt}</ref><?>{sparse signal}</?>

[refer] output the dense signal of the <ref>{prompt}</ref><?>{sparse signal}</?> in the image.

[refer] from this image, provide the dense signal for <ref>{prompt}</ref><?>{sparse signal}</?>.

[refer] please provide the dense signal coordinate of this region: <ref>{prompt}</ref><?>{sparse signal}</?>

[refer] can you locate and provide the dense signal for <ref>{prompt}</ref><?>{sparse signal}</?> in the given image?

**Response:** <?>{dense signal}</?>

**Query for GGL (Turn 1):**

[refer] give me the dense signal of <ref>{prompt}</ref>

[refer] output the dense signal of the <ref>{prompt}</ref> in the image.

[refer] from this image, provide the dense signal for <ref>{prompt}</ref>.

[refer] please provide the dense signal coordinate of the region this sentence describes: <ref>{prompt}</ref>

[refer] can you locate and provide the dense signal for <ref>{prompt}</ref> in the given image?

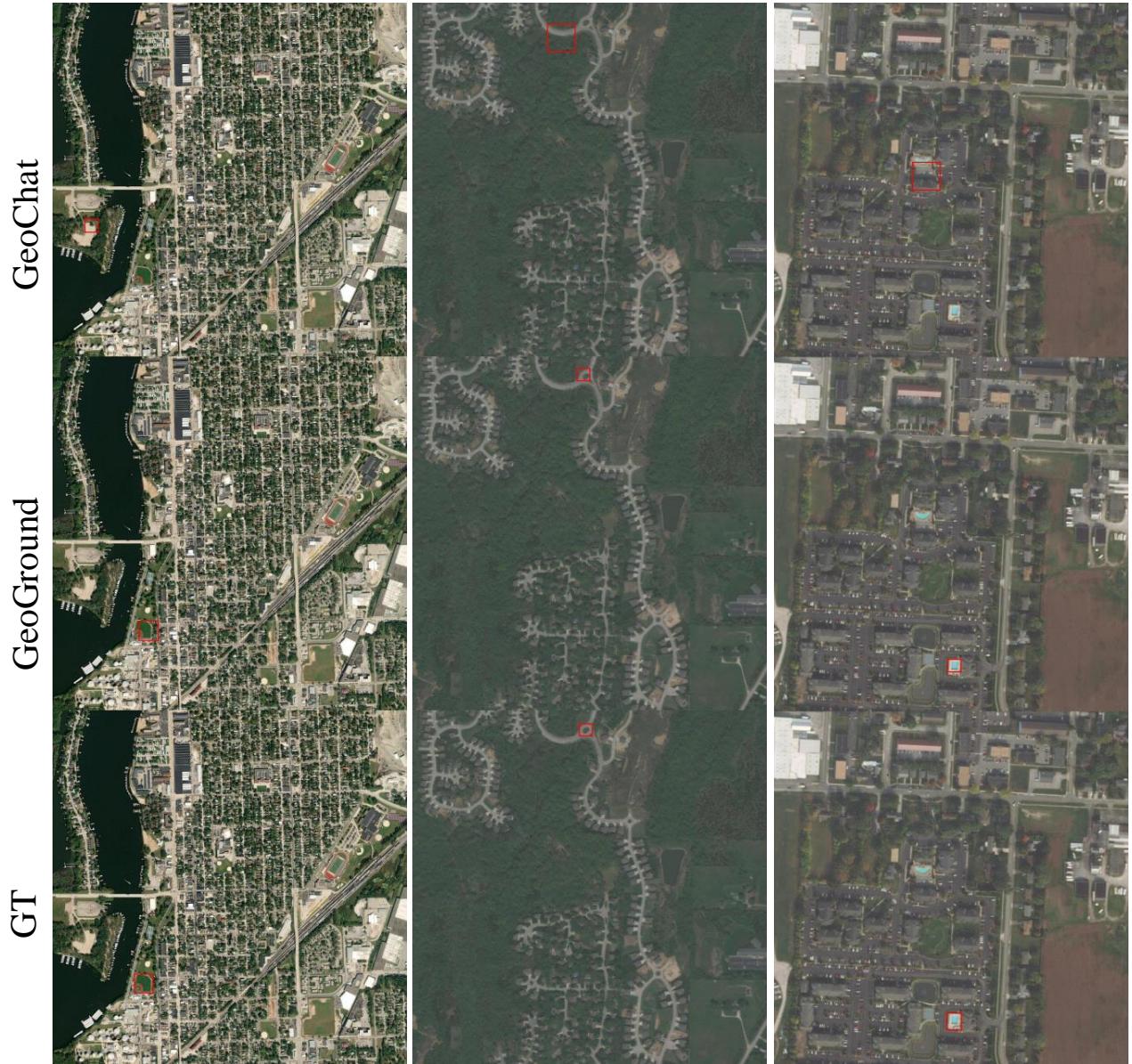
**Response:** <?>{dense signal}</?>

**Query for GGL (Turn 2):**

The sparse signal corresponding to this dense signal is

**Response:** <?>{sparse signal}</?>

Figure 10. The instruction fine-tuning template for GeoGround. The placeholder <?> can be replaced with <box>, <obb>, or <seg> depending on the specific situation.



the first baseball field that is about 8946 square meters in the south side of some baseball fields.

a roundabout that is about 537 square meters on the northernmost side.

a swimming pool that is about 457 square.

Figure 11. Visualizations of GeoGround and GeoChat on RSVG test set with HBB.

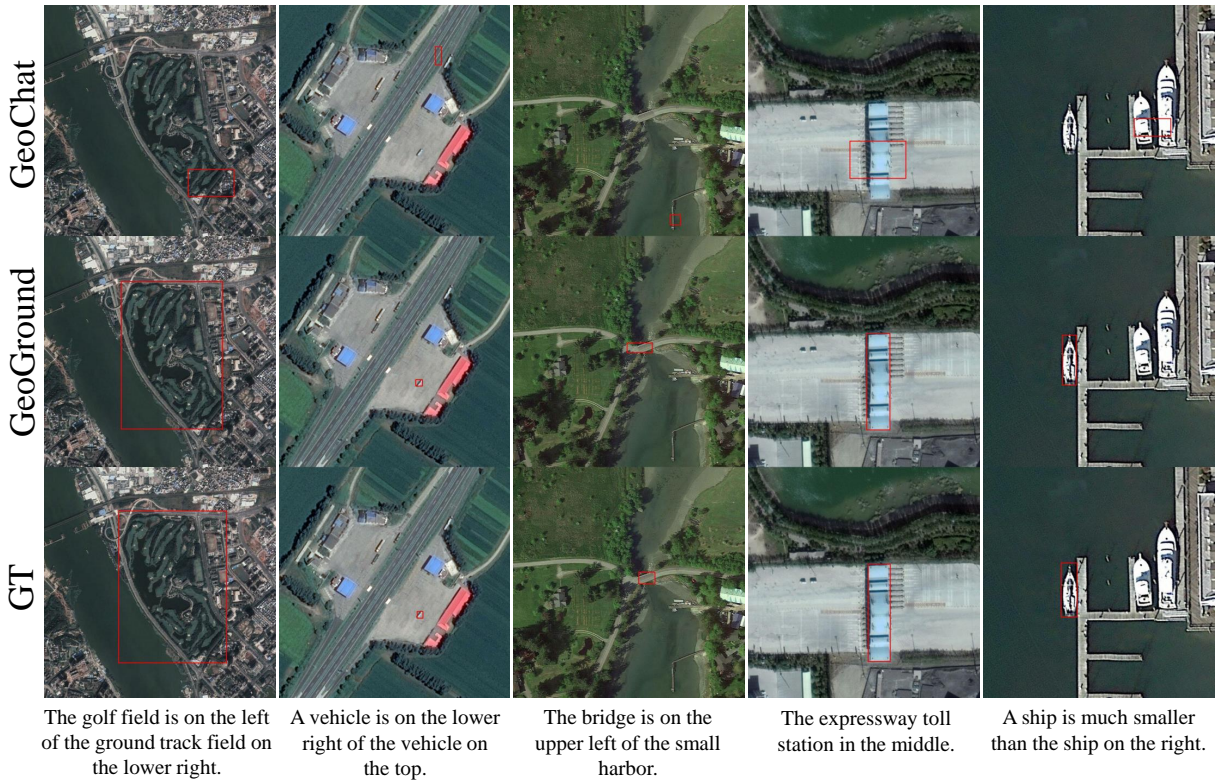


Figure 12. Visualizations of GeoGround and GeoChat on DOIR-RSVG test set with HBB.

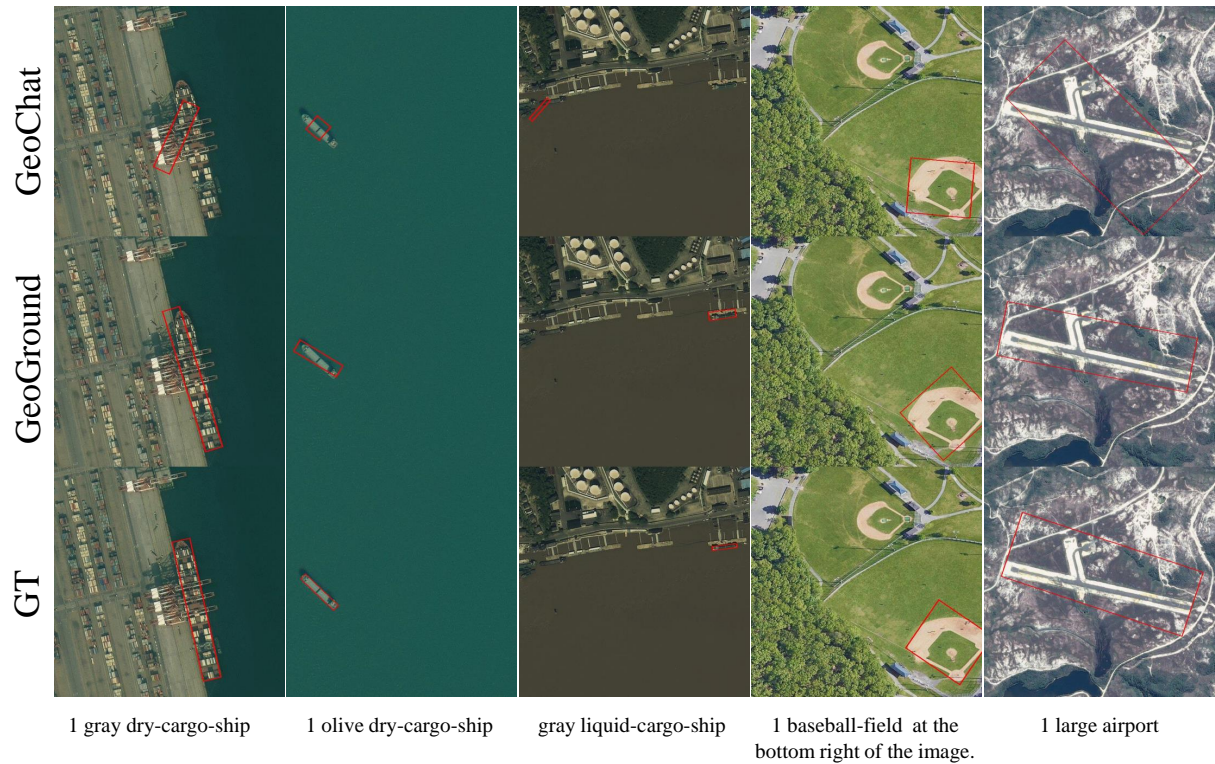


Figure 13. Visualizations of GeoGround and GeoChat on GeoChat test set with OBB. Compared to GeoChat, GeoGround, which adopts the le90 angle representation, provides more accurate predictions of the orientation of objects.

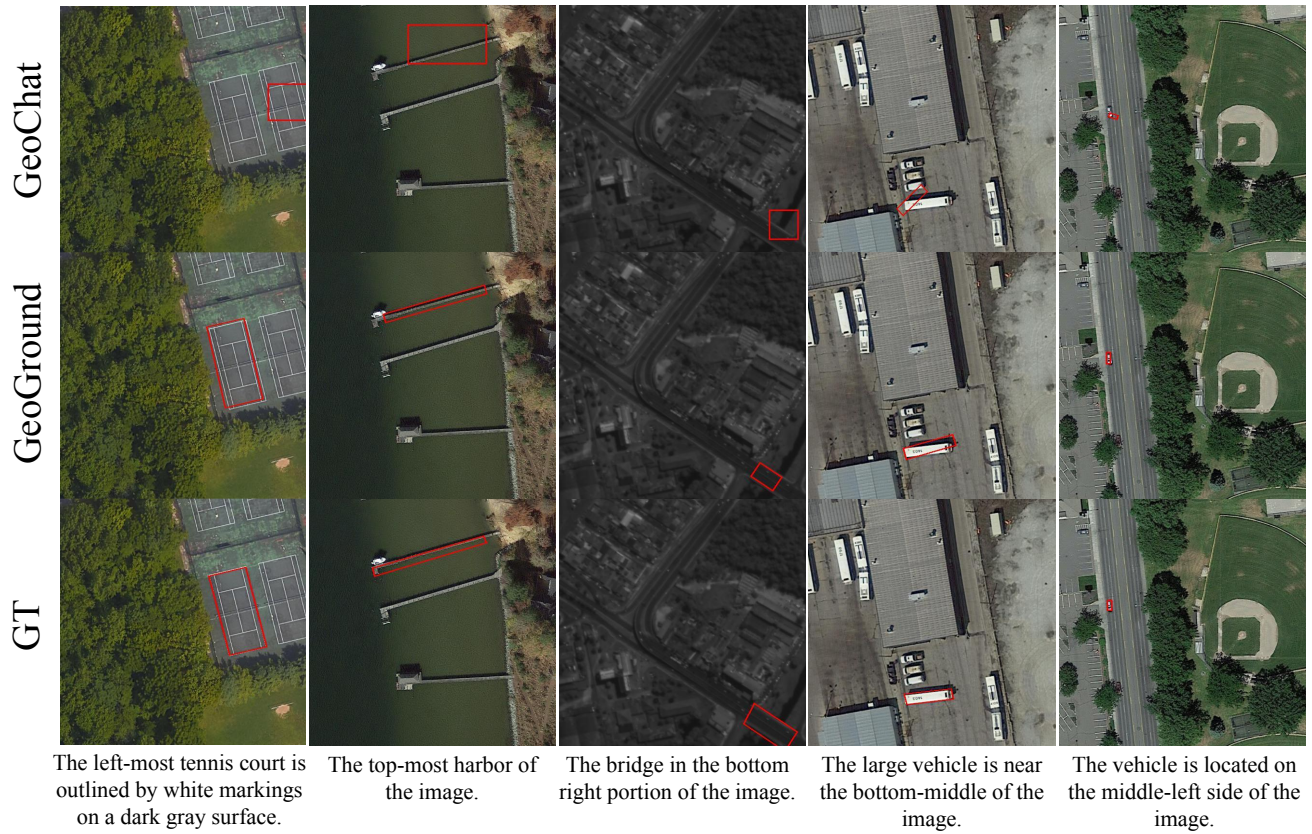


Figure 14. Visualizations of GeoGround and GeoChat on VRSBench test set with OBB.

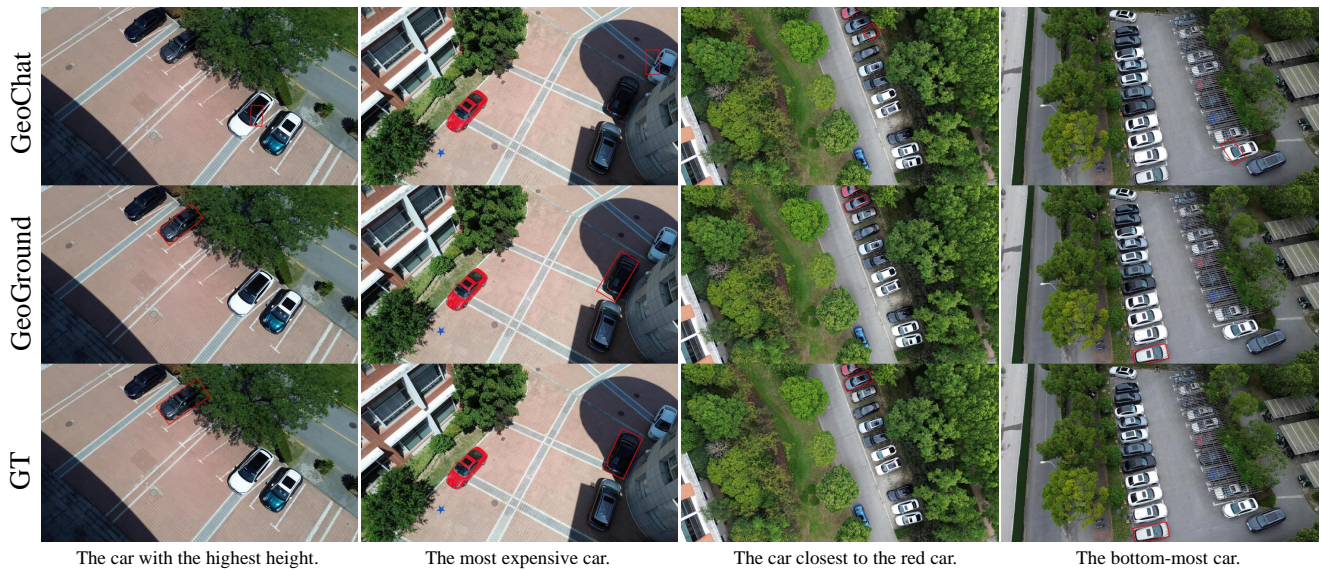
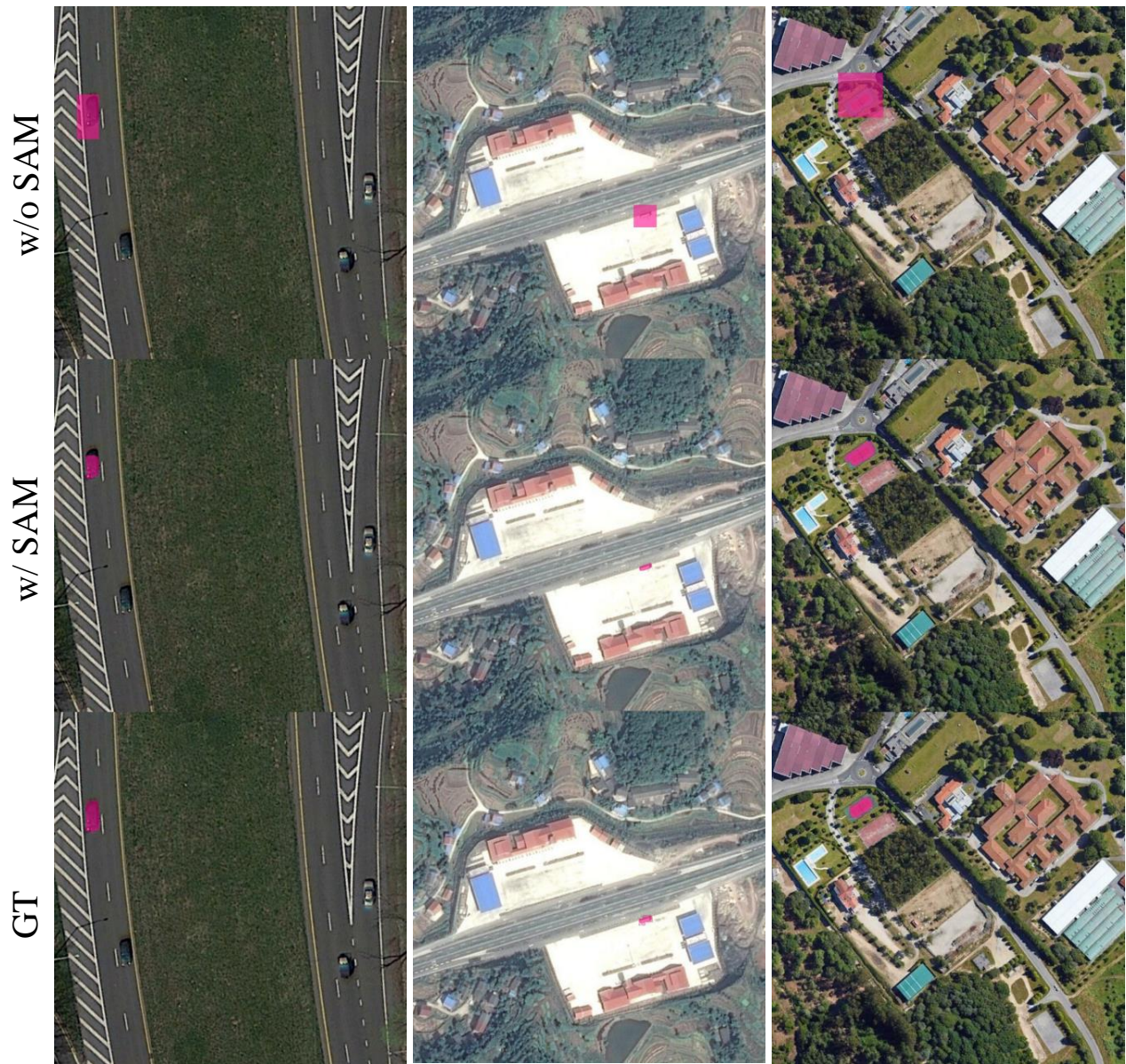


Figure 15. Visualizations of GeoGround and GeoChat on AVVG test set with OBB. GeoChat lacks spatial reasoning capabilities and is unable to infer the 3D space from its projection onto the 2D imaging plane.



The vehicle on the upper left.

A vehicle is parked in the expressway service area at the bottom.

A tennis court is on the gray vehicle on the top.

Figure 16. Visualization of GeoGround on RRSIS-D for tiny objects, with or without the SAM refiner. For tiny objects, the Matrix4Seg method is currently unable to accurately capture their shapes. Utilizing SAM as a refiner to fine-tune the masks is an effective approach.



Figure 17. Visualizations of GeoGround with and without SAM refiner on the RRSIS-D. The mask refiner can eliminate the mosaic artifacts introduced by Matrix4Seg, further improving the accuracy of the mask.

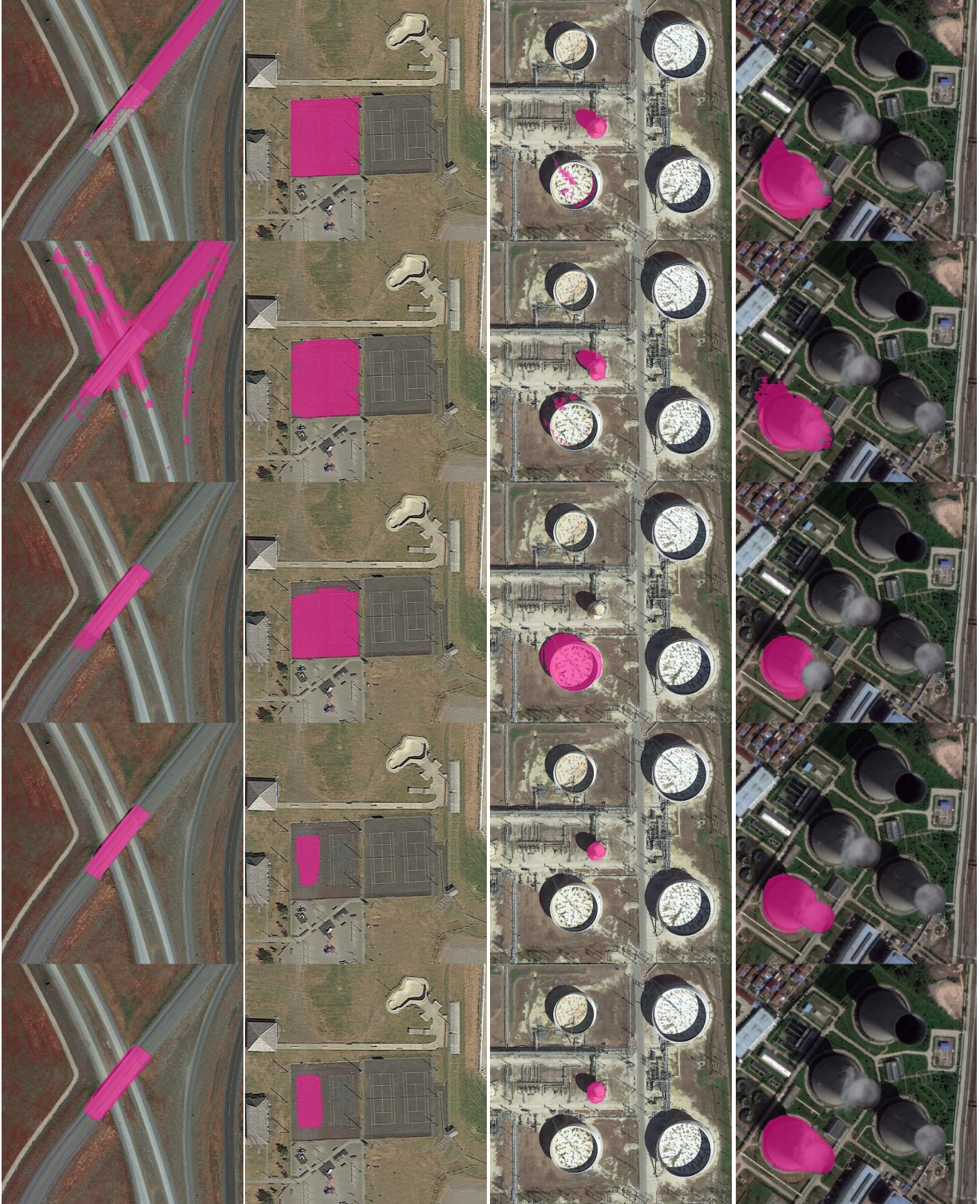
LISA

PixellLM

NExT-Chat

GeoGround + SAM

GT



A gray overpass.

The tennis court on the left.

The storage tank in the middle.

The chimney on the lower left.

Figure 18. Visualizations of GeoGround and other VLMs on the RRSIS-D.

LISA

PixellLM

NExT-Chat

GeoGround + SAM

GT



A windmill in the middle.



The ground track field on the left.



The stadium is on the left of the stadium at the bottom.



The tennis court at the bottom.

Figure 19. Visualizations of GeoGround and other VLMs on the RRSIS-D.



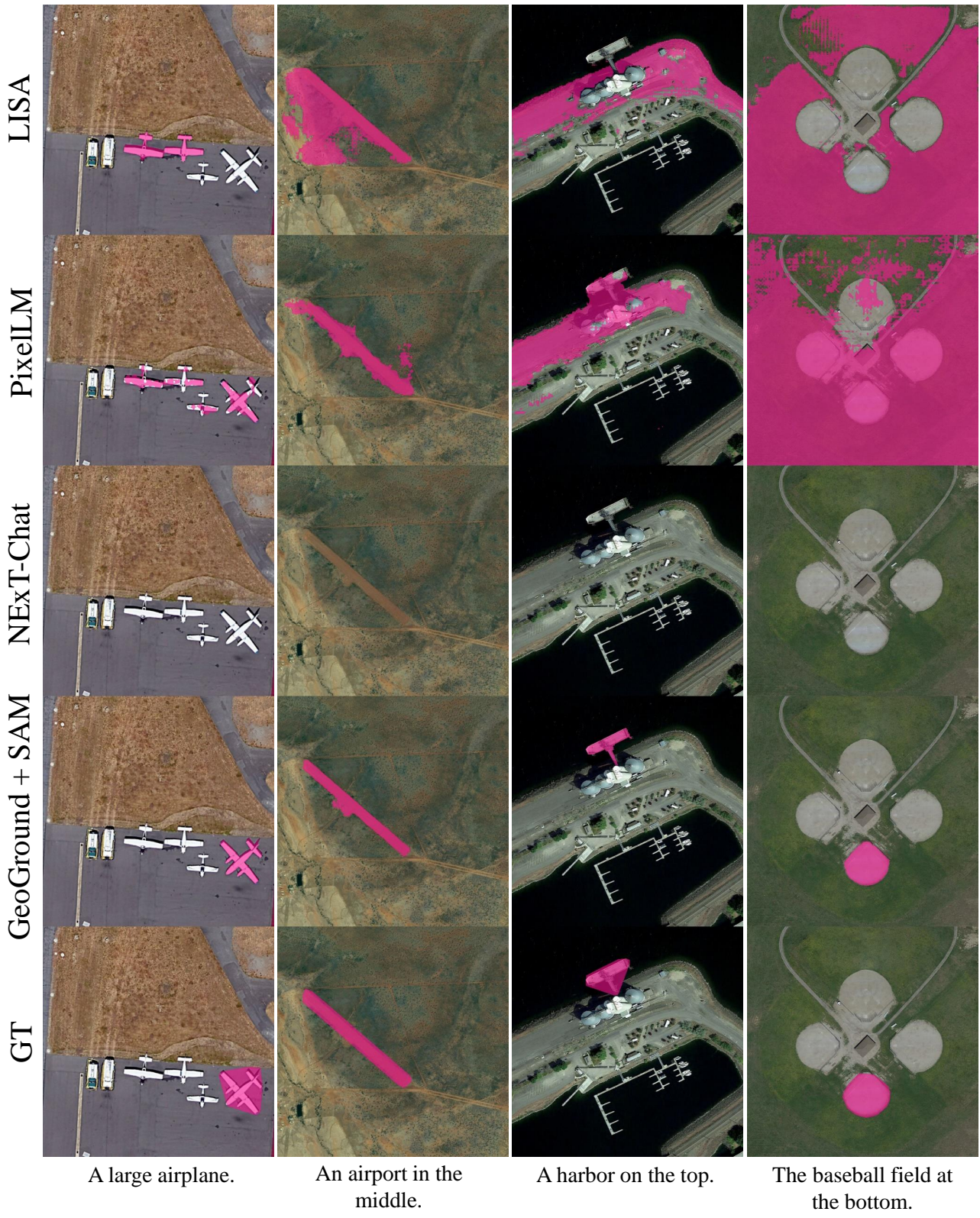


Figure 20. Visualizations of GeoGround and other VLMs on the RRSIS-D.